PAPER

Check for updates

Large second harmonic generation in a penta-CdO$_2$ sheet exfoliated from its bulk phase†

Changsheng Hou,[a] Yiheng Shen,[a] Qian Wang, [ID] *[a] Y. Kawazoe[bcd] and P. Jena [ID] [e]

Two-dimensional (2D) materials composed solely of pentagonal motifs are of particular interest due to their unique geometries and novel properties. Especially, the broken centrosymmetry and in-plane mirror symmetry in penta-graphene-like materials result in both in-plane and out-of-plane second harmonic generation (SHG). Transition metal cations with a filled d^{10} shell (d^{10}-TM) can significantly enhance the SHG response as found in many previously studied bulk materials. Here, based on first-principles calculations combined with independent particle approximation, we show that large SHG can also exist in some 2D d^{10}-TM oxides, such as penta-CdO$_2$, which can be chemically exfoliated from its bulk phase with its dynamical, thermal, and mechanical stability intact. We further find that penta-CdO$_2$ possesses extraordinary in-plane and out-of-plane SHG responses with large static SHG susceptibilities of $\chi^{\text{sheet}}_{14}(0) = \chi^{\text{sheet}}_{25}(0) = \chi^{\text{sheet}}_{36}(0) = 8.86$ pm^2 V^{-1} due to the phase-matching between fundamental and second-harmonic light. In addition, the low thermal expansion and a large optical band gap of 3.24 eV endow the penta-CdO$_2$ sheet with a high laser-induced damage threshold. Discussions are also made on the penta-ZnO$_2$ sheet. This study expands the family of 2D materials with outstanding SHG performance.

1. Introduction

Nonlinear optics has attracted significant interest due to its important role in photonic applications including ultrafast lasers,[1] frequency conversion,[2] photodetectors,[3] and optical modulator/switches/memories.[4] As one of the leading nonlinear optical responses, second harmonic generation (SHG) is one of the hotly pursued topics because it is more easily observed in experiments as compared to other higher-order nonlinear optical effects. In general, SHG materials are non-centrosymmetric and non-metallic. Therefore, even order terms can exist in their electric polarization expansion ($P = \varepsilon_0 \chi^{(2)} E^2 + \varepsilon_0 \chi^{(4)} E^4 + \ldots + \varepsilon_0 \chi^{(2n)} E^{2n}$). Since the few-atom thickness of the 2D materials is far below the coherence length of photons, the phase-matching condition is usually satisfied, making the SHG response strong enough for observation and utilization.[5] Thus, many non-centrosymmetric 2D materials with large SHG responses have been theoretically predicted and experimentally observed in recent years, including 2H-MoS$_2$,[6] h-BN,[7] 2D CrI$_3$,[8] 2D GaSe,[9] 2D SnSe,[10] 2D perovskite,[11] α-Sb and α-Bi.[12] In addition, the inversion symmetry of some centrosymmetric bulk materials is broken when thinned down to 2D materials, providing more opportunities to generate SHG responses.[13] However, the mirror symmetry in the out-of-plane direction hinders the out-of-plane components of the SHG matrix. For instance, odd-layer MoS$_2$ sheets with D_{3h} symmetry possess only one inequivalent in-plane SHG coefficient.[6] If the out-of-plane mirror symmetry could be broken, the SHG performance would be enhanced. Currently, one of the successful approaches to break the out-of-plane mirror symmetry for a remarkable out-of-plane SHG signal is to construct Janus structures, as in the case with α-In$_2$Se$_3$,[14] where the out-of-plane SHG susceptibility spectra enable ultrafast, simple, and noninvasive characterization of the vertical polarization, lattice symmetry, number of layers, and stacking sequence.

Compared with most 2D non-centrosymmetric materials constructed from highly symmetric hexagonal motifs, penta-graphene-like materials exhibit both in-plane and out-of-plane SHG responses, as found in penta-ZnS$_2$.[15] Since the theoretical prediction of penta-graphene,[16] over one hundred new pentagonal 2D materials have been theoretically proposed and some, experimentally synthesized.[17,18] It is interesting to note that the top-down approach has been successfully used for the synthesis of pentagonal 2D materials. For example, penta-PdSe$_2$ was

[a]*CAPT, School of Materials Science and Engineering, BKL-MEMD, Peking University, Beijing, 100871, China. E-mail: qianwang2@pku.edu.cn*

[b]*New Industry Creation Hatchery Center, Tohoku University, Sendai, 980-8577, Japan*

[c]*Department of Physics, Suranaree University of Technology, Nakhon Ratchasima, 30000, Thailand*

[d]*Department of Physics and Nanotechnology, SRM Institute of Science and Technology, Kattankulathur, Tamil Nadu, 603203, India*

[e]*Department of Physics, Virginia Commonwealth University, Richmond, VA, 23284, USA*

† Electronic supplementary information (ESI) available: Supporting information on the forty-five d^{10}-TM oxides from the Materials Project (MP) database, phonon spectra, SHG susceptibility, band-decomposed charge density distribution, optical band gap, optimized geometry, and electronic band structure. See DOI: https://doi.org/10.1039/d2ta07589j

This journal is © The Royal Society of Chemistry 2023

J. Mater. Chem. A, 2023, 11, 167–177 | **167**

prepared by exfoliating bulk $PdSe_2$ in the marcasite phase,[19] and penta-FeS_2 was synthesized by chemically cleaving bulk iron pyrite *via* liquid-phase exfoliation.[20] Thus, it is important to find new stable pentagonal sheets with extraordinary SHG performance that could potentially be synthesized from marcasite and pyrite materials. Techniques such as chemical vapor deposition[21] and molecular beam epitaxy[22] have also been used in the past to synthesize 2D pentagonal sheets. These include penta-$PdSe_2$, penta-silicene nanoribbon synthesized *via* physical vapor deposition,[23] penta-PdS_2 fabricated by sulfurization of a Pd film,[24] and penta-NiN_2 synthesized using a high-pressure approach.[25]

For the application in an optical device, high-quality SHG materials should satisfy several requirements including high SHG efficiency (a large static SHG susceptibility), moderate birefringence ($0.06 \leq \Delta n \leq 0.1$) to achieve phase-matching, and a high laser-induced damage threshold (LIDT) value in addition to high chemical and physical stabilities and easy-to-synthesize single crystals.[26] Since metal oxides have a strong absorption edge, and usually exhibit wide optical band gaps and high LIDT, they have received extensive attention in the design of high-performance SHG materials.[27] Since d^{10}-transition metal (d^{10}-TM) cations (*e.g.* Zn^{2+}, Cd^{2+}, Hg^{2+}, *etc.*) are electron rich, have flexible bonding, and possess polar displacement features, they can be expected to induce much larger polarizability and deformability, stimulating great interest in the design of bulk SHG materials containing d^{10}-TM.[28–32] Thus, it is possible that 2D d^{10}-TM oxides, entirely composed of pentagon motifs, would exhibit large SHG susceptibility, moderate birefringence to achieve phase-matching, and high LIDT. This expectation motivated us to carry out this study.

2. Computational methods

First-principles calculations are performed within the framework of density functional theory (DFT) implemented in the Vienna *Ab initio* Simulation Package (VASP).[33] The projected augmented wave (PAW)[34] method is used to treat interactions between ion cores and valence electrons. The Perdew–Burke–Ernzerhof (PBE) functional within the generalized gradient approximation (GGA)[35] is used to describe the electronic exchange–correlation interaction. The hybrid Heyd–Scuseria–Ernzerhof (HSE06)[36] functional is further applied to obtain accurate band structures. The energy cutoff, the convergence thresholds of total energy and inter-atomic force are set to

600 eV, 10^{-8} eV, and 10^{-6} eV Å^{-1}, respectively. The first Brillouin zone is represented by a $11 \times 11 \times 1$ k-point grid using the Monkhorst–Pack scheme.[37] The vacuum space is set to 18.28 Å in the nonperiodic direction to avoid interaction between two adjacent layers. The phonon spectra are calculated using the finite displacement method implemented in the Phonopy code[38] and a $5 \times 5 \times 1$ supercell. The temperature in *ab initio* molecular dynamics (AIMD) simulations is controlled by using the Nosé–Hoover thermostat.[39] The elastic constants are calculated using the finite difference methods.[40]

The SHG susceptibility is described by using a third-rank tensor $\chi_{abc}^{(2)}(-2\omega, \omega, \omega)$, defined as $P_a(2\omega) = \chi_{abc}^{(2)}(-2\omega, \omega, \omega)E_b(\omega)E_c(\omega)$, where $P(2\omega)$ is the second-order term of electric polarization, $E(\omega)$ is the fundamental light induced electric field, and $a, b, c \in \{x, y, z\}$. The $\chi_{abc}(\omega)$ is calculated within the independent particle approximation[41] by using the package developed by Zhang's group,[42] where the SHG tensor can be expressed by the sum of contributions from the pure inter-band process $\chi_{abc,e}(\omega)$ and the mixed inter-band and intra-band process $\chi_{abc,i}(\omega)$, both of which can be deduced from the electronic structure. The tensor component $\chi_{abc}^{\text{bulk}}(\omega)$ of a bulk material is calculated by using

$$\chi_{abc}^{\text{bulk}}(\omega) = \chi_{abc,e}^{\text{bulk}}(\omega) + \chi_{abc,i}^{\text{bulk}}(\omega). \tag{1}$$

Here, $\chi_{abc,e}^{\text{bulk}}(\omega)$ is the contribution from the pure inter-band contribution and has the following form,

$$\chi_{abc,e}^{\text{bulk}}(\omega) = \frac{e^3}{\hbar^2 \Omega} \sum_{nml,k} \frac{r_{nm}^a \{r_{nm}^a r_{ml}^b r_{ln}^c\}}{(\omega_{ln} - \omega_{ml})} \left[\frac{2f_{mn}}{\omega_{mn} - 2\omega} + \frac{f_{ln}}{\omega_{ln} - 2\omega} + \frac{f_{ml}}{\omega_{ml} - \omega} \right]. \tag{2}$$

$\chi_{abc,i}^{\text{bulk}}(\omega)$ is the contribution from the mixed inter-band and intra-band process that includes the modulation of linear polarization by the intra-band motion (the first three terms), and the intra-band motion modified by the polarization energy associated with inter-band motion of electrons (the last term).

$$\chi_{abc,i}^{\text{bulk}}(\omega) = \frac{i}{2} \frac{e^3}{\hbar^2 \Omega} \sum_{nm,k} f_{nm} \left[\begin{array}{c} \frac{2}{\omega_{mn}(\omega_{mn} - 2\omega)} r_{nm}^a (r_{nm;c}^b + r_{mn;b}^c) + \frac{1}{\omega_{mn}(\omega_{mn} - \omega)} (r_{nm;c}^a r_{mn}^b + r_{nm;b}^a r_{mn}^c) \\ + \frac{1}{\omega_{mn}^2} \left(\frac{1}{\omega_{mn} - \omega} - \frac{4}{\omega_{mn} - 2\omega} \right) r_{nm}^a (r_{mn}^b \Delta_{mn}^c + r_{mn}^c \Delta_{mn}^b) \\ - \frac{1}{2\omega_{mn}(\omega_{mn} - 2\omega)} (r_{nm;a}^b r_{mn}^c + r_{nm;a}^c r_{mn}^b) \end{array} \right]. \tag{3}$$

Here, Ω is the volume of the periodic cell, $f_{nm} = f_n - f_m$, $\omega_{nm} = \omega_n - \omega_m$, and $\Delta_{nm} = v_{nn} - v_{mm}$ are the differences of the Fermi distribution function, energy, and electron group velocity between the nth and mth bands, respectively. The operator $r_{mn}^a = p_{mn}^a/im\omega_{mn}$ is the position operator r_{mn} projected on axial directions, which can be derived from the momentum matrix component p_{mn}. $\{r_{nl}^b r_{lm}^a\}$ is defined as $1/2(r_{nl}^b r_{lm}^a + r_{nl}^a r_{lm}^b)$.

$r_{nm;a}{}^b$ is the generalized derivative of the coordinate operator in momentum space and has the form,

$$r_{nm;a}{}^b = \frac{r_{nm}{}^a \Delta_{mn}{}^b + r_{nm}{}^b \Delta_{mn}{}^a}{\omega_{nm}} + \frac{i}{\omega_{nm}} \sum_l \left(\omega_{lm} r_{ln}{}^a r_{lm}{}^b - \omega_{nl} r_{nl}{}^b r_{lm}{}^a \right).$$

(4)

The static SHG susceptibility can be obtained by using the Kramers–Kronig transformation,[43]

$$\chi_{abc}^{bulk}(0) = \text{Re}\left[\chi_{abc}^{bulk}(0)\right] = \frac{2}{\pi} P \int_0^\infty \left\{ \text{Im}\left[\chi_{abc}^{bulk}(\omega)\right]/\omega \right\} d\omega.$$

(5)

To obtain a converged SHG susceptibility tensor, the electronic structures are calculated at the PBE level with a very dense k-point sampling of $99 \times 99 \times 1$. Since the PBE/GGA underestimates the band gap in the calculation of optical properties, the scissor approximation is applied where the difference between the band gaps is obtained at the PBE and HSE06 levels in SHG calculations.[44] For 2D materials, it is necessary to replace the volume Ω in eqn (2) and (3) with the area of the 2D plane of the unit cell, as the volume depends on the thickness of the vacuum space in the normal direction of 2D materials.[10] Thus, the unit of the sheet SHG susceptibility χ_{abc}^{sheet} is $pm^2 V^{-1}$.

The linear optical properties of bulk materials are obtained from the complex frequency-dependent dielectric function $\varepsilon_{ij}^{bulk}(\omega)$. The imaginary part $\text{Im}[\varepsilon_{ij}^{bulk}(\omega)]$ is calculated by using the following equation:[45]

$$\text{Im}\left[\varepsilon_{ij}^{bulk}(\omega)\right] = \frac{2e^2\pi}{\Omega \varepsilon_0} \sum_{k,v,c} \left| \langle \psi_k^c | \hat{u} \times r | \psi_k^v \rangle \right|^2 \delta\left(E_k^c - E_k^v - E\right).$$

(6)

Here, u and e represent the incident electric field and elementary charge, while $\psi_k c$ and ψ_k^v denote the conduction band and valence band wave function at the given k point, respectively. The real part $\text{Re}[\varepsilon_{ij}^{bulk}(\omega)]$ is obtained from the imaginary part based on the Kramers–Kronig dispersion relation:[46]

$$\text{Re}\left[\varepsilon_{ij}^{bulk}(\omega)\right] = 1 + \frac{2}{\pi} P \int_0^\infty \frac{\omega'^2 \text{Im}\left[\varepsilon_{ij}^{bulk}(\omega)\right]}{\omega'^2 - \omega^2} d\omega'.$$

(7)

Here, P denotes the principal value.

The real and imaginary dielectric functions of 2D materials also need to be renormalized due to the thickness-dependent volume Ω in eqn (6). Therefore, we use the following formulae[47] to calculate the dielectric functions of the penta-CdO$_2$ sheet $\varepsilon_{ij}^{sheet}(\omega)$:

$$\text{Re}\left[\varepsilon_{ij}^{sheet}(\omega)\right] = 1 + \frac{L_z}{L_z^{eff}} \left\{ \text{Re}\left[\varepsilon_{ij}^{bulk}(\omega)\right] - 1 \right\}.$$

(8)

$$\text{Im}\left[\varepsilon_{ij}^{sheet}(\omega)\right] = \frac{L_z}{L_z^{eff}} \text{Im}\left[\varepsilon_{ij}^{bulk}(\omega)\right].$$

(9)

Here, L_z is the cell length along the normal direction of the sheet, and L_z^{eff} is the effective length, which is determined as the sum of the van der Waals thickness (3.4 Å on each side of the sheet) and the thickness (d_{2D}) of the 2D material *via* the equation, $L_z^{eff} = 3.4 \text{ Å} \times 2 + d_{2D}$. Tests for the thickness independence of our calculated SHG susceptibility and dielectric function are carried out. The details can be found in Fig. S1 in the ESI.†

3. Results and discussion

3.1 Structure and stability

The 2D frameworks featuring the Cairo pentagonal tessellation exist in the marcasite and pyrite materials with *Pnnm* symmetry (space group no. 58), and *Pa$\bar{3}$* symmetry (space group no. 206), respectively.[48] Hence, it is possible to obtain the corresponding pentagon-based sheets by using physical or chemical exfoliation techniques. We rationally search for pentagonal d^{10}-TM oxide sheets from their bulk counterparts containing internal pentagonal layers. The searching starts from an initial set of crystals extracted from the Materials Project (MP) database,[49] retrieving entries with one d^{10}-TM element and oxygen, where we only consider the compounds matching the experimentally determined materials in the Inorganic Crystal Structure Database (ICSD).[50] Under these conditions, the initial dataset provides 45 bulk structures for further analysis, as summarized in Table S1 in the ESI.† Then, according to the features of the marcasite and pyrite unit cells, we use the space group symmetry (*Pnnm*, *Pbca* or *Pa$\bar{3}$*), the stoichiometry (1 : 2 or 2 : 1), and 12 atoms per unit cell as descriptors to identify bulk materials with a pentagonal configuration. These combined criteria reduce the original set of the 45 bulk structures to 3 structures (ZnO$_2$, CdO$_2$, and HgO$_2$). We then directly extract pentagonal sheets from the bulk materials. The fully optimized geometries of the pentagonal sheets extracted from bulk ZnO$_2$ and CdO$_2$ exhibit a penta-graphene-like configuration with $P\bar{4}2_1m$ symmetry (space group no. 113), which are termed as penta-ZnO$_2$ and penta-CdO$_2$, respectively. The fully optimized pentagonal sheet extracted from bulk HgO$_2$ possesses a penta-PdSe$_2$-like[19] configuration with $P2_1/c$ symmetry (space group no. 14), which is named penta-HgO$_2$. In the next step, we obtain their phonon spectra to check their dynamic stabilities. The results plotted in Fig. S2† show that penta-ZnO$_2$, penta-CdO$_2$ and penta-HgO$_2$ are all dynamically stable as no any imaginary modes are found in the first Brillouin zones of their phonon spectra. Only the penta-graphene-like configuration of pentagon-based sheets can exhibit both in-plane and out-of-plane SHG responses.[15] The other two typical types including penta-PdSe$_2$-like and penta-NiN$_2$-like[25] configurations are centrosymmetric, which do not meet the basic requirements to exhibit SHG, thus reducing the original set of the three structures to two stable structures, namely, penta-ZnO$_2$ and penta-CdO$_2$. Since the difference in electronegativity of Cd and O atoms (1.75) is smaller than that of Zn and O atoms (1.79), the Cd–O bond is more covalent than the Zn–O bond, and the electrons in the Cd–O bond are expected to exhibit a stronger response under an electric field than that in the Zn–O bond, implying a stronger SHG response in penta-CdO$_2$. Hence, we choose the penta-CdO$_2$ sheet for further investigation. More details on penta-ZnO$_2$ can be found in the ESI.†

This journal is © The Royal Society of Chemistry 2023

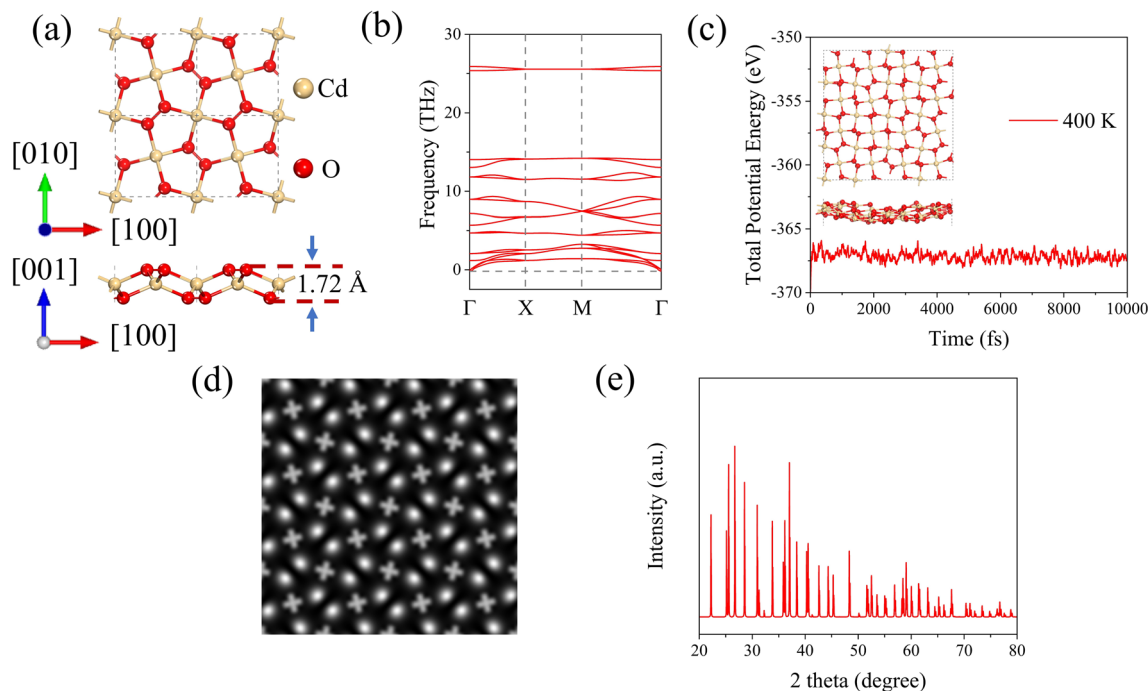*J. Mater. Chem. A*, 2023, **11**, 167–177 | **169**

Fig. 1 (a) Top and side views of the optimized geometry, and (b) phonon spectrum of penta-CdO$_2$. (c) Total potential energy fluctuation of penta-CdO$_2$ with time during the AIMD simulation at 400 K. (d) Simulated constant height STM image with bias voltage $V_{bias} = -1$ mV, and (e) simulated XRD pattern of the penta-CdO$_2$ sheet.

The optimized geometry and phonon spectrum of the penta-CdO$_2$ sheet are presented in Fig. 1(a and b). The unit cell contains two Cd and four O atoms, which occupy two nonequivalent Wyckoff positions, namely, 2b (0.500, 0.500, and 0.500) and 4e (0.605, 0.105, and 0.543), respectively. Its lattice parameters are $a = b = 5.00$ Å. The Cd–O, and O–O bond lengths are 2.22 Å and 1.49 Å, respectively. The buckling height of the penta-CdO$_2$ sheet is 1.72 Å. To explore the feasibility of its experimental synthesis, we calculate the exfoliation energies of the monolayer and bilayer penta-CdO$_2$, which are defined as

$$E_{exf}(n) = \left[E_{iso}(n) - \frac{n}{m}E_{bulk} \right] \Big/ A. \tag{10}$$

Here, $E_{exf}(n)$, $E_{iso}(n)$, and E_{bulk} denote the exfoliation energy, the energy of the exfoliated sheet, and the energy of the bulk material, respectively. The parameters n, m and A are the number of layers in the exfoliated sheet and the bulk material, and the surface area of the bulk material, respectively. The calculated exfoliation energies of the monolayer and bilayer penta-CdO$_2$ are 0.85 J m^{-2} and 0.12 J m^{-2}, which are comparable to those of graphene[51] (0.37 J m^{-2}) and phosphorene[52] (0.35 J m^{-2} for the monolayer and 0.37 J m^{-2} for the bilayer), indicating that it is possible to obtain the penta-CdO$_2$ sheet from its bulk counterpart.

The thermal stability of penta-CdO$_2$ is examined by performing AIMD simulations at 400 K. The duration of the simulation is 10 ps with a time step of 1 fs. To ensure that the observed stability is not caused by the constraints of periodic boundary conditions, a $4 \times 4 \times 1$ supercell is used in the simulations. As shown in Fig. 1(c), the total potential energy fluctuates slightly around a constant value during the

simulation and the geometry does not suffer significant distortion at the end of the simulation, which indicates that the penta-CdO$_2$ sheet is thermally stable at 400 K.

The simulated scanning tunneling microscopy (STM) image is graphically plotted as shown in Fig. 1(d). One can see that some O–O dimers are brighter than the others, reflecting the buckled feature of this sheet. The simulated X-ray diffraction (XRD) of penta-CdO$_2$ is also carried out, which is presented in Fig. 1(e). Finally, we examine the mechanical stability of penta-CdO$_2$. The calculated linear elastic constants are $C_{11} = 28.67$ N m^{-1}, $C_{12} = -0.86$ N m^{-1}, and $C_{66} = 13.72$ N m^{-1}. These values satisfy the requirements of Born–Huang criteria,[53] namely, $C_{11} > 0$, $C_{11} > C_{12}$ and $C_{66} > 0$ for 2D materials, confirming that penta-CdO$_2$ is mechanically stable.

3.2 Mechanical properties

Having confirmed the stability of penta-CdO$_2$, we study the mechanical properties of penta-CdO$_2$ based on its linear elastic constants. The in-plane Young's modulus (E) and Poisson's ratio (v) along an arbitrary direction (θ) are deduced from the following formulae:[54]

$$E(\theta) = \frac{C_{11}^2 - C_{12}^2}{C_{11}(s^4 + c^4) + \left(\frac{C_{11}^2 - C_{12}^2}{C_{66}} - 2C_{12} \right)c^2s^2}, \tag{11}$$

$$v(\theta) = -\frac{\left(2C_{11} - \frac{C_{11}^2 - C_{12}^2}{C_{66}} \right)c^2s^2 - C_{12}(c^4 + s^4)}{C_{11}(s^4 + c^4) + \left(\frac{C_{11}^2 - C_{12}^2}{C_{66}} - 2C_{12} \right)c^2s^2}. \tag{12}$$
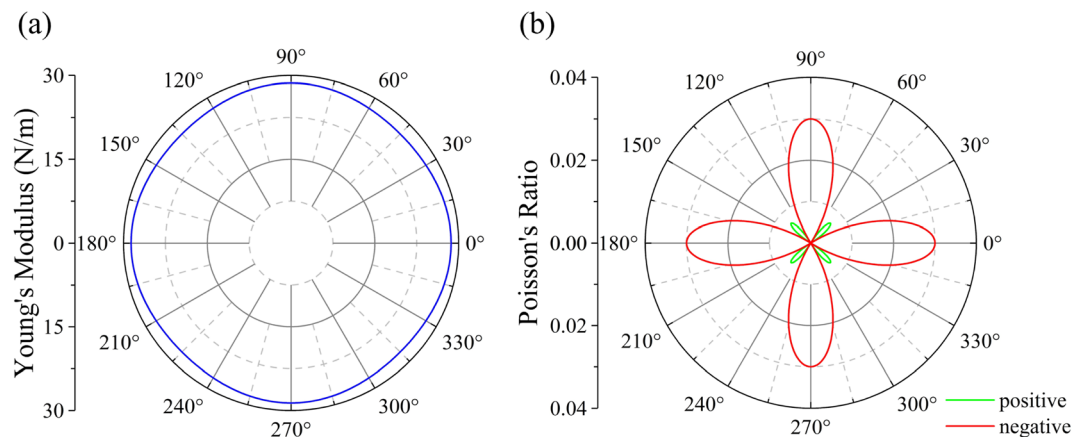
Fig. 2 Variation of (a) the in-plane Young's modulus, and (b) Poisson's ratio with the direction in penta-CdO$_2$.

Here, $s = \sin\theta$, $c = \cos\theta$, and θ represents the in-plane angle with respect to the [100] direction. As shown in Fig. 2(a), the Young's modulus E shows weak anisotropy, and its maximum value is 28.64 N m^{-1} along the [100] direction, which is only about 8% that of graphene (345 N m^{-1}).[55] The Poisson ratio ν of penta-CdO$_2$ is highly anisotropic, exhibiting butterfly-like characteristics. Interestingly, we note that C_{12} is negative for penta-CdO$_2$, leading to a negative Poisson's ratio (NPR) along most directions. The largest value of a positive Poisson's ratio is 0.01 along the [110] and its equivalent directions, while the largest absolute value of a negative Poisson's ratio is -0.03 along the [100] and its equivalent directions. Therefore, penta-CdO$_2$ with NPR may have applications in nanomechanical devices as a nano-auxetic material.

3.3 Electronic properties

The electronic properties of penta-CdO$_2$ are studied by calculating its band structure and corresponding total and partial density of states (DOS) at the HSE06 level, and the results are plotted and shown in Fig. 3(a). The band structure calculated at the PBE level is also given for comparison. One can see that penta-CdO$_2$ is semiconducting with an indirect bandgap of 1.54 eV at the PBE level, as the valence band maximum (VBM)

and conduction band minimum (CBM) are located at different points along the M–Γ path in the first Brillouin zone. The electronic band structure at the HSE06 level has a similar dispersion but with a larger band gap of 3.28 eV due to the well-known fact that the PBE functional underestimates the band gaps. The partial DOS (PDOS) shows that the VBM is mainly contributed by the O atoms, while the CBM comes from both the Cd and O atoms.

Next, we calculate the electron localization function (ELF)[56] for this sheet. The ELF is a dimensionless parameter normalized in the range [0.0, 1.0], where 0.0 corresponds to a low electron density, 1.0 corresponds to fully localized electrons and 0.5 corresponds to completely delocalized electrons, as shown in Fig. 3(b). One can see that the ELF values in the vicinity of the O–O dimers (yellow and orange clouds) are in between 0.5 and 1.0, indicating that these electrons exhibit a covalent nature. The free electrons (green cloud) surrounding the O–O dimers being separated by the blue regions with low charge density further confirm the semiconducting feature of the penta-CdO$_2$ sheet. Using the Bader charge analysis,[57,58] we find that each Cd atom transfers 1.21 electrons to each of the O–O dimers, which is larger than that in the penta-ZnS$_2$ sheet[15] (0.88 electrons). Hence, the electrons of O–O dimers in penta-CdO$_2$ are more
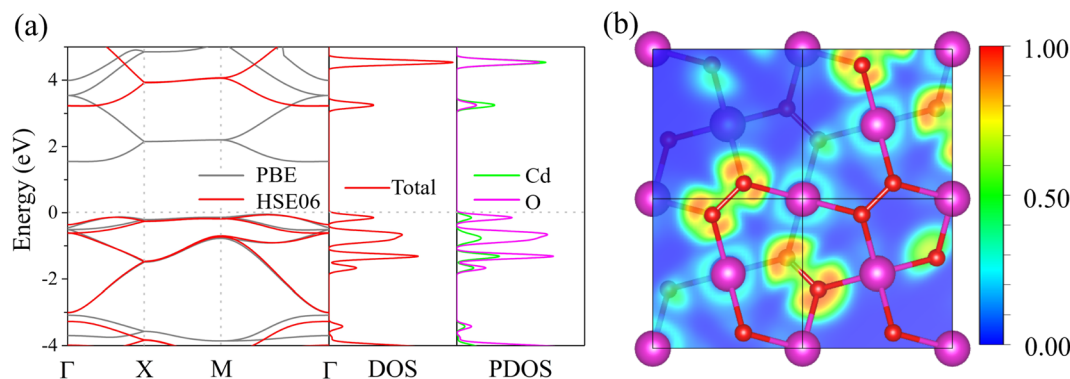

Fig. 3 (a) Electronic band structure, and total and partial DOS of penta-CdO$_2$. (b) ELF distribution on the plane formed by the ∠O–O–Cd in penta-CdO$_2$.

delocalized than those of S–S dimers in penta-ZnS$_2$, indicating that the electrons of O–O dimers can exhibit a more obvious response under an electric field, leading to a strong SHG response in penta-CdO$_2$.

3.4 SHG susceptibility

We then evaluate the SHG properties of penta-CdO$_2$. Because the penta-CdO$_2$ sheet belongs to $P\bar{4}2_1m$ symmetry (space group no. 113), only two independent nonzero components $\chi_{xyz}^{\text{sheet}}(\omega) = \chi_{yxz}^{\text{sheet}}(\omega)$ and $\chi_{zxy}^{\text{sheet}}(\omega)$ are allowed by the symmetry constraints, which are further reduced to $\chi_{14}^{\text{sheet}}(\omega) = \chi_{25}^{\text{sheet}}(\omega)$ and $\chi_{36}^{\text{sheet}}(\omega)$ under the Voigt notation.[59] These tensor components show a crossover between the direction of the SHG response and the incident electric field, where the out-of-plane electric field contributes to the in-plane polarization via $\chi_{14}^{\text{sheet}}(\omega)$ and $\chi_{25}^{\text{sheet}}(\omega)$, and the in-plane electric field is also necessary for the out-of-plane polarization via $\chi_{36}^{\text{sheet}}(\omega)$. Hence, penta-CdO$_2$ can exhibit both in-plane and out-of-plane SHG susceptibilities. To compensate for the underestimated band gap at the PBE level, we use the scissor correction of the band gap difference $\Delta = 1.74$ eV in the calculations of SHG for higher accuracy.[44] Besides, we find that the SHG properties converge at a k-point mesh of $99 \times 99 \times 1$, which is illustrated in Fig. S3.†

Next, we calculate the static SHG susceptibilities of penta-CdO$_2$, which are the zero-frequency limit of the SHG susceptibilities. The static SHG susceptibilities satisfy Kleinman's symmetry, where only one independent value $\chi_{14}^{\text{sheet}}(0) = \chi_{25}^{\text{sheet}}(0) = \chi_{36}^{\text{sheet}}(0) = 8.86$ pm^2 V^{-1} exists in penta-CdO$_2$, which is much larger than that of penta-ZnS$_2$ [$\chi_{14}^{\text{sheet}}(0) = \chi_{36}^{\text{sheet}}(0) = -1.22$ pm^2 V^{-1}, $\chi_{31}^{\text{sheet}}(0) = \chi_{15}^{\text{sheet}}(0) = 0.69$ pm^2 V^{-1}].[15] In addition, to compare with the results of the SHG of bulk materials, the sheet SHG susceptibility $\chi_{abc}^{\text{sheet}}(\omega)$ of 2D materials can be converted to the corresponding bulk SHG susceptibility $\chi_{abc}^{\text{bulk}}(\omega)$ via the equation $\chi_{abc}^{\text{sheet}}(\omega) = \chi_{abc}^{\text{bulk}}(\omega) \times L_z^{\text{eff}}$, where L_z^{eff} is the effective length used for the correction of the dielectric function. The converted static bulk SHG susceptibility $\chi_{14}\text{bulk}(0) = \chi_{25}\text{bul}^{\text{k}}(0) = \chi_{36}\text{bulk}(0)$ of penta-CdO$_2$ is 1.04 pm V^{-1}, which is about twice that of the well-known KBBF [experimental value of 0.47 pm V^{-1} at a low photon energy of $\omega = 1.17$ eV,[60] while our calculated value is 0.45 pm V^{-1}, as presented in Fig. S4 in the ESI†]. Such large static SHG susceptibility indicates a strong frequency-doubling effect in penta-CdO$_2$, which is promising for optical device applications.

To study the thickness dependence of the SHG of penta-CdO$_2$, we carry out calculations for the bilayer and trilayer penta-CdO$_2$ sheets using the Grimme's semiempirical van der Waals correction (DFT-D3).[61] The AA-stacking configuration is found to be the most stable for the bilayer penta-CdO$_2$ sheet (see Fig. S5†). On the other hand, the optimized trilayer penta-CdO$_2$ (see Fig. S6†) undergoes a phase transition toward its bulk pyrite phase without an SHG response due to the $Pa\bar{3}$ centro-symmetry with the space group of no. 206. Thus, we only focus on the bilayer configuration. The static SHG susceptibility of bilayer penta-CdO$_2$ is calculated to be $\chi_{14}^{\text{sheet}}(0) = \chi_{25}^{\text{sheet}}(0) = \chi_{36}^{\text{sheet}}(0) = 13.17$ pm^2 V^{-1}, which is larger than the value of the penta-CdO$_2$ sheet [$\chi_{14}^{\text{sheet}}(0) = \chi_{25}^{\text{sheet}}(0) = \chi_{36}^{\text{sheet}}(0) = 8.86$ pm^2 V^{-1}]. The
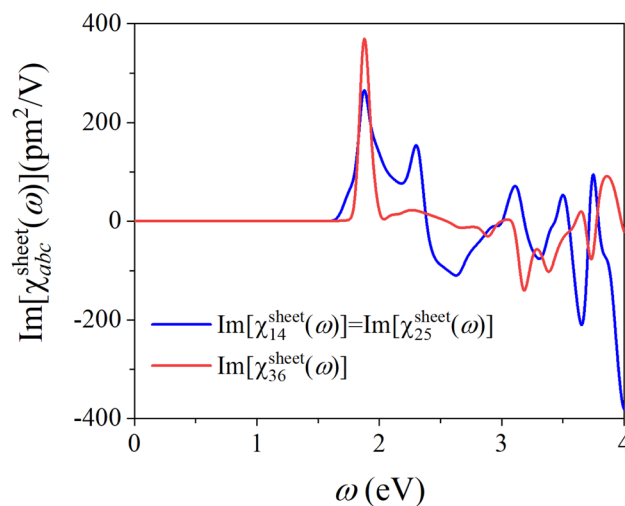

Fig. 4 Imaginary part of the SHG susceptibilities of penta-CdO$_2$.

calculated results for the SHG susceptibility of the bilayer penta-CdO$_2$ sheet are plotted and shown in Fig. S7 in the ESI.†

Next, we calculate the frequency-dependent SHG susceptibility of penta-CdO$_2$, especially considering its imaginary part ($\text{Im}[\chi_{abc}^{\text{sheet}}(\omega)]$). The imaginary parts of different nonzero independent SHG tensor components are plotted and shown in Fig. 4, while the real parts and modulus are plotted in Fig. S8.† Unlike previously reported 2D materials with a major in-plane SHG response,[10] the penta-CdO$_2$ sheet has both strong in-plane and out-of-plane SHG responses. One can see that Im $[\chi_{14}^{\text{sheet}}(\omega)]$ and $\text{Im}[\chi_{36}^{\text{sheet}}(\omega)]$ have the most significant peak value of 264.12 pm^2 V^{-1} and 368.92 pm^2 V^{-1} at 1.88 eV, respectively. From eqn (5), it can be inferred that the low-energy region of Im $[\chi_{abc}^{\text{sheet}}(\omega)]$ primarily determines the value of $\chi_{abc}^{\text{sheet}}(0)$ due to the existence of denominator ω in the integrand. Hence, the first several peaks in $\text{Im}[\chi_{abc}^{\text{sheet}}(\omega)]$ make dominant contributions to $\chi_{abc}^{\text{sheet}}(0)$. For reference, the most significant peak Im $[\chi_{36}^{\text{sheet}}(\omega)]$ value in penta-ZnS$_2$ is -13.76 pm^2 V^{-1} at 3.19 eV, which is pushed away from the low energy range due to its larger band gap of 3.34 eV. Thus, the larger value of the most significant peak in penta-CdO$_2$ and its larger contribution lead to a larger $\chi_{abc}^{\text{sheet}}(0)$ value as compared to that in penta-ZnS$_2$. In addition, all of the major peaks in $\text{Im}[\chi_{abc}^{\text{sheet}}(\omega)]$ of penta-CdO$_2$ are located within the photon energy range of 1.63–3.10 eV (400–760 nm), showing good visible nonlinear optical properties.

For the SHG response in a semiconductor, the light-induced electric polarization ($P = \sum p + \int tj \mathrm{d}t$) includes two main physical contributions, which are the inter-band contribution (a dipole moment p created by a pure inter-band transition) and intra-band contribution (a polarization current j generated by electrons moving within their original bands driven by the E-field). We calculate the contribution from different mechanisms to the $\text{Im}[\chi_{abc}^{\text{sheet}}(\omega)]$ of penta-CdO$_2$. As shown in Fig. 5(a and b), we plot the different contributions to the imaginary part of SHG in penta-CdO$_2$. We see that the inter-band and intra-band contributions to each SHG susceptibility tend to oppose each other,

172 | J. Mater. Chem. A, 2023, 11, 167–177

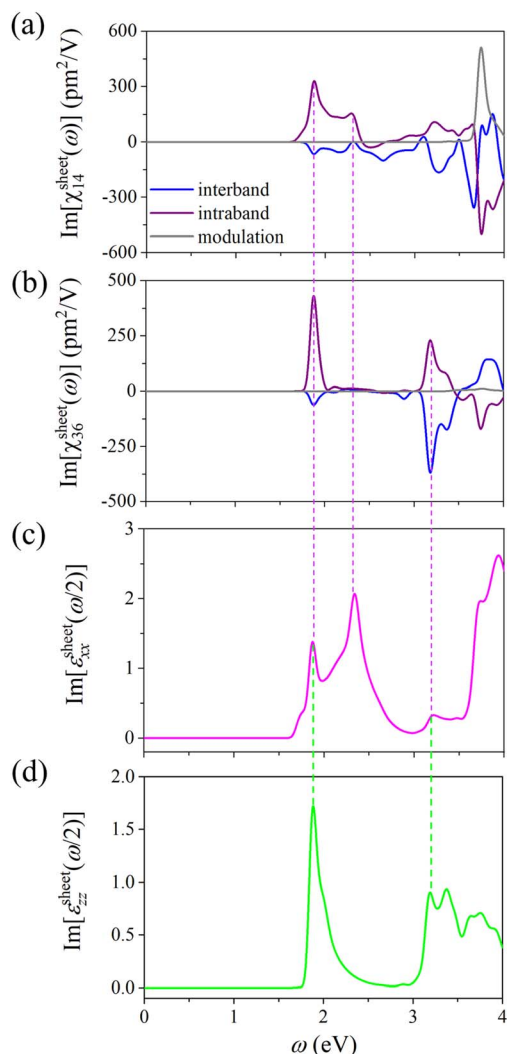This journal is © The Royal Society of Chemistry 2023

Fig. 5 Imaginary parts (a) $\text{Im}[\chi_{14}^{\text{sheet}}(\omega)]$ and (b) $\text{Im}[\chi_{36}^{\text{sheet}}(\omega)]$ of the inter-band, intra-band and modulation for the SHG susceptibility, and the imaginary part of the dielectric function (c) $\text{Im}[\varepsilon_{xx}^{\text{sheet}}(\omega/2)]$ and (d) $\text{Im}[\varepsilon_{zz}^{\text{sheet}}(\omega/2)]$ of penta-CdO$_2$.

and the major peaks are mostly contributed by the intra-band term. Hence, the intra-band contribution to each SHG susceptibility is larger in magnitude compared to that from the inter-band contribution.

We then calculate the imaginary part of the dielectric function $\text{Im}[\varepsilon_{xx}^{\text{sheet}}(\omega/2)]$ and $\text{Im}[\varepsilon_{zz}^{\text{sheet}}(\omega/2)]$ at the PBE level using an identical k-point mesh in the SHG calculations. The calculated results are plotted and shown in Fig. 5(c and d). To explore the connection between the SHG properties and the linear optical properties of penta-CdO$_2$, the mutual extrema in $\text{Im}[\chi_{abc}^{\text{sheet}}(\omega)]$ and $\text{Im}[\varepsilon_{ij}^{\text{sheet}}(\omega/2)]$ are marked in Fig. 5 by the dashed lines. One can see that the major peak of $\text{Im}[\chi_{14}^{\text{sheet}}(\omega)]$ and $\text{Im}[\chi_{36}^{\text{sheet}}(\omega)]$ at 1.88 eV is related to both $\text{Im}[\varepsilon_{xx}^{\text{sheet}}(\omega/2)]$ and $\text{Im}[\varepsilon_{zz}^{\text{sheet}}(\omega/2)]$. On the other hand, the minor peak of $\text{Im}[\chi_{14}^{\text{sheet}}(\omega)]$ at 2.35 eV is related to $\text{Im}[\varepsilon_{xx}^{\text{sheet}}(\omega/2)]$. Because SHG is a two-photon process, the incident light with frequencies of both 2ω and ω can induce resonance for a band

energy difference of $2\hbar\omega$. For penta-CdO$_2$, the spectra of $\text{Im}[\varepsilon_{ij}^{\text{sheet}}(\omega/2)]$ exhibit significant absorption peaks at $\omega = 3.76$, 4.70, and 6.40 eV, respectively. Hence, the peaks in $\text{Im}[\chi_{abc}^{\text{sheet}}(\omega)]$ at $\omega = 1.88$, 2.35, and 3.20 eV are induced by two-photon resonance, indicating a strong SHG response. Meanwhile, the k-point-dependent distributions of dielectric functions are used to analyze the connection between the SHG properties and the band structure, which are illustrated in Fig. S9.† Here, we focus on the peaks of $\text{Im}[\varepsilon_{xx}^{\text{sheet}}(\omega/2)]$ and $\text{Im}[\varepsilon_{zz}^{\text{sheet}}(\omega/2)]$ at $\omega/2 = 1.88$ eV, which are both relevant to that of $\text{Im}[\chi_{14}^{\text{sheet}}(\omega)]$ and $\text{Im}[\chi_{36}^{\text{sheet}}(\omega)]$. One can see that the main contributions to $\text{Im}[\varepsilon_{xx}^{\text{sheet}}(\omega/2)]$ and $\text{Im}[\varepsilon_{zz}^{\text{sheet}}(\omega/2)]$ are from the transitions at the high symmetry point M and the M–Γ path. We further decompose the summed-up contribution from all band-to-band transitions at each k-point to particular band-to-band transitions. The major contribution to the peak value of $\text{Im}[\varepsilon_{xx}^{\text{sheet}}(\omega/2)]$ is from the degenerate VBM-2-CBM and VBM-3-CBM+1 transitions at the high symmetry point M, and that of $\text{Im}[\varepsilon_{zz}^{\text{sheet}}(\omega/2)]$ is mainly from the VBM-2-CBM transition along the M–Γ path. These are marked by pink and green arrows in Fig. S9(c).† It is also worth mentioning that the excited electron tends to transfer from the negatively charged O atoms to the positively charged Cd atoms, as shown in the band decomposed charge density in Fig. S10,† implying that the electronic states of the Cd–O bonds are the origin of the strong SHG susceptibility of penta-CdO$_2$.

3.5 Phase-matching

In addition to the SHG susceptibility, phase-matching is another crucial factor for high-quality SHG materials. This is closely related to the incident laser wavelength.[62] To show the phase-matching behavior of penta-CdO$_2$, we calculate the refractive index n and birefringence Δn by using the previously calculated dielectric function ε_{xx} and ε_{zz}. The refractive index n is obtained according to the formula:[63]

$$n_{ij}(\omega) = \frac{1}{\sqrt{2}}\left[\left|\varepsilon_{ij}^{\text{sheet}}(\omega)\right| + \text{Re}\left[\varepsilon_{ij}^{\text{sheet}}(\omega)\right]\right]^{\frac{1}{2}}. \quad (13)$$

Here, $i,j = 1$, 2, and 3 correspond to the x, y, and z directions of the Cartesian coordinates and $\text{Re}[\varepsilon_{xx}^{\text{sheet}}(\omega)]$ and $\text{Im}[\varepsilon_{xx}^{\text{sheet}}(\omega)]$ are the real and imaginary parts of the dielectric function, respectively. Besides, birefringence (Δn) is calculated as $\Delta n = \max|n_i - n_j|$, $i \neq j$. As shown in Fig. 6(a), the calculated refractive indices (n) indicate that the $n_z(n_e)$ values of penta-CdO$_2$ are smaller than $n_x = n_y(n_o)$, where n_x, n_y, and n_z are the refractive indices along the x, y, and z directions, and n_e and n_o are refractive indices of extraordinary and ordinary light, respectively. Hence, the penta-CdO$_2$ sheet is a negative uniaxial crystal. On the basis of the type-I phase-matching conditions of $n_e(2\omega) = n_o(\omega)$, where ω and 2ω refer to fundamental and second-harmonic light, respectively, the wavelength limit for penta-CdO$_2$ is 682 nm, which occurs in the visible light range. One can see that the birefringence is around 0.06 in Fig. 6(b), exhibiting moderate birefringence ($0.06 \leq \Delta n \leq 0.1$).[26] This indicates that the fundamental and second-harmonic light exhibit phase-matching when propagating in this sheet, so that the SHG
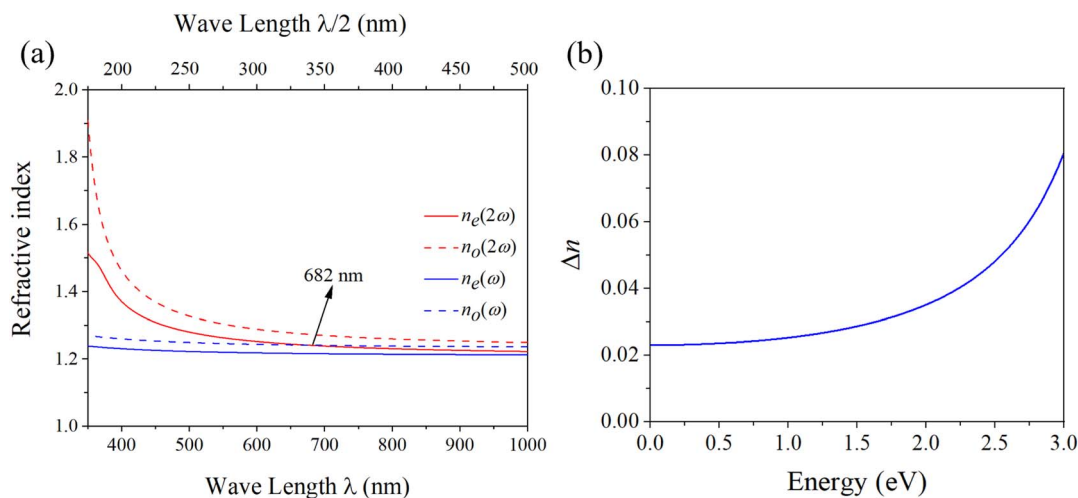
This journal is © The Royal Society of Chemistry 2023

J. Mater. Chem. A, 2023, **11**, 167–177 | **173**

Fig. 6 (a) Wavelength-dependent refractive indices and (b) energy-dependent birefringence of penta-CdO$_2$.

response can be enhanced. As generally accepted, the laser-induced damage threshold of a material is influenced by several factors, including the optical band gap, thermal expansion, physical and chemical stability, crystal quality, *etc.*[64] Among these, the optical band gap is generally the main factor for both single crystal and polycrystalline samples.[62] As shown in Fig. S11(a),† we use Tauc plot methodology to obtain the optical band gap of the penta-CdO$_2$ sheet, which is shown as follows:[65]

$$(\alpha h\nu)^n = K(h\nu - E_g). \tag{14}$$

In this equation, α is the absorption coefficient, $h\nu$ is the incident photon energy, K is an energy independent constant, and E_g is the optical band gap. Besides, for a direct band gap material $n = 2$, while for an indirect material $n = 1/2$. The calculated optical band gap of penta-CdO$_2$ is 3.24 eV, indicating high LIDT for penta-CdO$_2$. Note that only the SHG signal below the minimal band pair energy of 3.24 eV is considered in the above analysis, because of the dominant linear optical absorption beyond this limit. We also calculate the thermal expansion from 0 K to 400 K of penta-CdO$_2$ by using the quasi harmonic approximation method[66] as implemented in the Phonopy code.[38] The results are plotted and shown in Fig. S11(b).† The low thermal expansion also favors its high LIDT.

4. Conclusions

In summary, the SHG performance of 2D d^{10}-TM oxides, the penta-CdO$_2$ sheet, is studied for the first time using first-principles calculations combined with independent particle approximation. We show that the penta-CdO$_2$ sheet can be chemically exfoliated from its bulk phase with a low exfoliation energy of 0.85 J m^{-2}, and is dynamically, thermally and mechanically stable. Penta-CdO$_2$ is semiconducting with an indirect band gap of 3.28 eV at the HSE06 level, and possesses a negative Poisson's ratio of $\nu_{12} = \nu_{21} = C_{12}/C_{11} = -0.03$. More

interestingly, it exhibits both in-plane and out-of-plane static SHG susceptibilities with a value of $\chi_{14}^{\text{sheet}}(0) = \chi_{25}^{\text{sheet}}(0) = \chi_{36}^{\text{sheet}}(0) = 8.86$ pm^2 V^{-1}, which is larger than that of penta-ZnS$_2$ [$\chi_{14}^{\text{sheet}}(0) = \chi_{36}^{\text{sheet}}(0) = -1.22$ pm^2 V^{-1}, $\chi_{31}^{\text{sheet}}(0) = \chi_{15}^{\text{sheet}}(0) = 0.69$ pm^2 V^{-1}]. The $\text{Im}[\chi_{14}^{\text{sheet}}(\omega)]$ and $\text{Im}[\chi_{36}^{\text{sheet}}(\omega)]$ have the most significant peak values of 264.12 pm^2 V^{-1} and 368.92 pm^2 V^{-1} at 1.88 eV, respectively, showing good visible nonlinear optical properties. The low thermal expansion together with a large optical band gap of 3.24 eV makes penta-CdO$_2$ promising for a high laser-induced damage threshold. In addition, we extend this study to the penta-ZnO$_2$ sheet, another 2D d^{10}-TM oxide, which also exhibits a large SHG response: $\chi_{14}^{\text{sheet}}(0) = \chi_{25}^{\text{sheet}}(0) = \chi_{36}^{\text{sheet}}(0) = -5.60$ pm^2 V^{-1}. We hope that these intriguing features will stimulate experimental efforts in the synthesis of such 2D pentagonal materials for the applications in nano-SHG devices.

Conflicts of interest

There are no conflicts to declare.

Acknowledgements

174 | *J. Mater. Chem. A*, 2023, **11**, 167–177

This journal is © The Royal Society of Chemistry 2023

University (Japan) for their continuous support of the MASAMUNE-IMR supercomputing facility.

References

1 U. Keller, Recent developments in compact ultrafast lasers, *Nature*, 2003, **424**, 831–838.

2 D. Cyranoski, Materials science: China's crystal cache, *Nature*, 2009, **457**, 953–955.

3 F. Zhou, I. Abdelwahab, K. Leng, K. P. Loh and W. Ji, 2D Perovskites with giant excitonic optical nonlinearities for high-performance sub-bandgap photodetection, *Adv. Mater.*, 2019, **31**, 1904155.

4 Z. Sun, A. Martinez and F. Wang, Optical modulators with 2D layered materials, *Nat. Photonics*, 2016, **10**, 227–238.

5 M. Zhao, Z. Ye, R. Suzuki, Y. Ye, H. Zhu, J. Xiao, Y. Wang, Y. Iwasa and X. Zhang, Atomically phase-matched second-harmonic generation in a 2D crystal, *Light: Sci. Appl.*, 2016, **5**, e16131.

6 Y. Li, Y. Rao, K. F. Mak, Y. You, S. Wang, C. R. Dean and T. F. Heinz, Probing symmetry properties of few-layer MoS_2 and h-BN by optical second-harmonic generation, *Nano Lett.*, 2013, **13**, 3329–3333.

7 C. J. Kim, L. Brown, M. W. Graham, R. Hovden, R. W. Havener, P. L. McEuen, D. A. Muller and J. Park, Stacking order dependent second harmonic generation and topological defects in h-BN bilayers, *Nano Lett.*, 2013, **13**, 5660–5665.

8 Z. Sun, Z. Yi, T. Song, G. Clark, B. Huang, Y. Shan, S. Wu, D. Huang, C. Gao, Z. Chen, M. McGuire, T. Cao, D. Xiao, W. T. Liu, W. Yao, X. Xu and S. Wu, Giant nonreciprocal second-harmonic generation from antiferromagnetic bilayer CrI_3, *Nature*, 2019, **572**, 497–501.

9 X. Zhou, J. Cheng, Y. Zhou, T. Cao, H. Hong, Z. Liao, S. Wu, H. Peng, K. Liu and D. Yu, Strong second-harmonic generation in atomic layered GaSe, *J. Am. Chem. Soc.*, 2015, **137**, 7994–7997.

10 H. Wang and X. Qian, Giant optical second harmonic generation in two-dimensional multiferroics, *Nano Lett.*, 2017, **17**, 5027–5034.

11 W. J. Wei, X. X. Jiang, L. Y. Dong, W. W. Liu, X. B. Han, Y. Qin, K. Li, W. Li, Z. S. Lin, X. H. Bu and P. X. Lu, Regulating second-harmonic generation by van der waals interactions in two-dimensional lead halide perovskite nanosheets, *J. Am. Chem. Soc.*, 2019, **141**, 9134–9139.

12 Y. Guo, H. Zhu and Q. Wang, Large second harmonic heneration in elemental α-Sb and α-Bi monolayers, *J. Phys. Chem. C*, 2020, **124**, 5506–5513.

13 F. Liu, W. Wu, Y. Bai, S. H. Chae, Q. Li, J. Wang, J. Hone and X. Y. Zhu, Disassembling 2D van der waals crystals into macroscopic monolayers and reassembling into artificial lattices, *Science*, 2020, **367**, 903–906.

14 L. Hu and X. Huang, Peculiar electronic, strong in-plane and out-of-plane second harmonic generation and piezoelectric properties of atom-thick α-M_2X_3 (M = Ga, In; X = S, Se): role of spontaneous electric dipole orientations, *RSC Adv.*, 2017, **7**, 55034–55043.

15 Y. Shen, Y. Guo and Q. Wang, Large out-of-plane second harmonic generation susceptibility in penta-ZnS_2 sheet, *Adv. Theory Simul.*, 2020, **3**, 2000027.

16 S. Zhang, J. Zhou, Q. Wang, X. Chen, Y. Kawazoe and P. Jena, Penta-graphene: a new carbon allotrope, *Proc. Natl. Acad. Sci. U. S. A.*, 2015, **112**, 2372–2377.

17 M. A. Nazir, A. Hassan, Y. Shen and Q. Wang, Research progress on penta-graphene and its related materials: Properties and applications, *Nano Today*, 2022, **44**, 101501.

18 Y. Shen and Q. Wang, Pentagon-based 2D materials: Classification, properties and applications, *Phys. Rep.*, 2022, **964**, 1–42.

19 A. D. Oyedele, S. Yang, L. Liang, A. A. Puretzky, K. Wang, J. Zhang, P. Yu, P. R. Pudasaini, A. W. Ghosh, Z. Liu, C. M. Rouleau, B. G. Sumpter, M. F. Chisholm, W. Zhou, P. D. Rack, D. B. Geohegan and K. Xiao, $PdSe_2$: Pentagonal two-dimensional layers with high air stability for electronics, *J. Am. Chem. Soc.*, 2017, **139**, 14090–14097.

20 A. B. Puthirath, A. P. Balan, E. F. Oliveira, V. Sreepal, F. C. R. Hernandez, G. Gao, N. Chakingal, L. M. Sassi, P. Thibeorchews, G. Costin, R. Vajtai, D. S. Galvao, R. R. Nair and P. M. Ajayan, Apparent ferromagnetism in exfoliated ultrathin pyrite sheets, *J. Phys. Chem. C*, 2021, **125**, 18927–18935.

21 Y. Gu, H. Cai, J. Dong, Y. Yu, A. N. Hoffman, C. Liu, A. D. Oyedele, Y. C. Lin, Z. Ge, A. A. Puretzky, G. Duscher, M. F. Chisholm, P. D. Rack, C. M. Rouleau, Z. Gai, X. Meng, F. Ding, D. B. Geohegan and K. Xiao, Two-dimensional palladium diselenide with strong in-plane optical anisotropy and high mobility grown by chemical vapor deposition, *Adv. Mater.*, 2020, **32**, 1906238.

22 E. Li, D. Wang, P. Fan, R. Zhang, Y. Y. Zhang, G. Li, J. Mao, Y. Wang, X. Lin, S. Du and H. J. Gao, Construction of bilayer $PdSe_2$ on epitaxial graphene, *Nano Res.*, 2018, **11**, 5858–5865.

23 J. I. Cerdá, J. Sławińska, G. L. Lay, A. C. Marele, J. M. G. Rodríguez and M. E. Dávila, Unveiling the pentagonal nature of perfectly aligned single and double strand Si nano-ribbons on Ag(110), *Nat. Commun.*, 2016, **7**, 13076.

24 X. Zhang, G. Su, J. Lu, W. Yang, W. Zhuang, K. Han, X. Wang, Y. Wan, X. Yu and P. Yang, Centimeter scale few-layer PdS_2: Fabrication and physical properties, *ACS Appl. Mater. Interfaces*, 2021, **13**, 43063–43074.

25 M. Bykov, E. Bykova, A. V. Ponomareva, F. Tasnádi, S. Chariton, V. B. Prakapenka, K. Glazyrin, J. S. Smith, M. F. Mahmood, I. A. Abrikosov and A. F. Goncharov, Realization of an ideal Cairo tessellation in nickel diazenide NiN_2: High-pressure route to pentagonal 2D materials, *ACS Nano*, 2021, **15**, 13539–13546.

26 K. M. Ok, E. O. Chi and P. S. Halasyamani, Bulk characterization methods for non-centrosymmetric materials: Second-harmonic generation, piezoelectricity, pyroelectricity, and ferroelectricity, *Chem. Soc. Rev.*, 2006, **35**, 710–717.

27 C. Wu, X. Jiang, L. Lin, Y. Hu, T. Wu, Z. Lin, Z. Huang, M. G. Humphrey and C. Zhang, A congruent-melting mid-infrared nonlinear optical vanadate exhibiting strong

This journal is © The Royal Society of Chemistry 2023

J. Mater. Chem. A, 2023, **11**, 167–177 | **175**

second-harmonic generation, *Angew. Chem., Int. Ed.*, 2021, **60**, 22447–22453.

28 H. Yu, H. Wu, S. Pan, Z. Yang, X. Hou, X. Su, Q. Jing, K. R. Poeppelmeier and J. M. Rondinelli, $Cs_3Zn_6B_9O_{21}$: A chemically benign member of the KBBF family exhibiting the largest second harmonic generation response, *J. Am. Chem. Soc.*, 2014, **136**, 1264–1267.

29 C. Hu, B. Zhang, B. H. Lei, S. Pan and Z. Yang, Advantageous units in antimony sulfides: Exploration and design of infrared nonlinear optical materials, *ACS Appl. Mater. Interfaces*, 2018, **10**, 26413–26421.

30 Z. Xie, M. Mutailipu, G. He, G. Han, Y. Wang, Z. Yang, M. Zhang and S. Pan, A series of rare-earth borates $K_7MRE_2B_{15}O_{30}$ (M = Zn, Cd, Pb; RE = Sc, Y, Gd, Lu) with Large Second Harmonic Generation Responses, *Chem. Mater.*, 2018, **30**, 2414–2423.

31 J. A. Brant, D. J. Clark, Y. S. Kim, J. I. Jang, J. H. Zhang and J. A. Aitken, Li_2CdGeS_4, A diamond-like semiconductor with strong second-order optical nonlinearity in the infrared and exceptional laser damage threshold, *Chem. Mater.*, 2014, **26**, 3045–3048.

32 X. Dong, L. Huang, H. Zeng, Z. Lin, K. M. Ok and G. Zou, High-performance sulfate optical materials exhibiting giant second harmonic generation and large birefringence, *Angew. Chem., Int. Ed.*, 2022, **134**, e202116790.

33 G. Kresse and J. Furthmüller, Efficient iterative schemes for *ab initio* total-energy calculations using a plane-wave basis set, *Phys. Rev. B: Condens. Matter Mater. Phys.*, 1996, **54**, 11169–11186.

34 P. E. Blöchl, Projector augmented-wave method, *Phys. Rev. B: Condens. Matter Mater. Phys.*, 1994, **50**, 17953–17979.

35 J. P. Perdew, K. Burke and M. Ernzerhof, Generalized gradient approximation made simple, *Phys. Rev. Lett.*, 1996, **77**, 3865–3868.

36 J. Heyd, G. E. Scuseria and M. Ernzerhof, Hybrid functionals based on a screened coulomb potential, *J. Chem. Phys.*, 2003, **118**, 8207–8215.

37 H. J. Monkhorst and J. D. Pack, Special points for Brillouin-zone integrations, *Phys. Rev. B: Condens. Matter Mater. Phys.*, 1976, **13**, 5188–5192.

38 A. Togo, F. Oba and I. Tanaka, First-principles calculations of the ferroelastic transition between rutile-type and $CaCl_2$-type SiO_2 at high pressures, *Phys. Rev. B: Condens. Matter Mater. Phys.*, 2008, **78**, 134106.

39 C. Braga and K. P. Travis, A configurational temperature Nosé-Hoover thermostat, *J. Chem. Phys.*, 2005, **123**, 134101.

40 X. Wu, D. Vanderbilt and D. R. Hamann, Systematic treatment of displacements, strains, and electric fields in density-functional perturbation theory, *Phys. Rev. B: Condens. Matter Mater. Phys.*, 2005, **72**, 035105.

41 J. E. Sipe and E. Ghahramani, Nonlinear optical response of semiconductors in the independent-particle approximation, *Phys. Rev. B: Condens. Matter Mater. Phys.*, 1993, **48**, 11705–11722.

42 Z. Fang, J. Lin, R. Liu, P. Liu, Y. Li, X. Huang, K. Ding, L. Ning and Y. Zhang, Computational design of inorganic nonlinear

optical crystals based on a genetic algorithm, *CrystEngComm*, 2014, **16**, 10569–10580.

43 S. N. Rashkeev and W. R. L. Lambrecht, Second-harmonic generation of I-III-VI$_2$ halcopyrite semiconductors: Effects of chemical substitutions, *Phys. Rev. B: Condens. Matter Mater. Phys.*, 2001, **63**, 165212.

44 Z. H. Levine and D. C. Allan, Calculation of the nonlinear susceptibility for optical second-harmonic generation in III-V semiconductors, *Phys. Rev. Lett.*, 1991, **66**, 41–44.

45 Q. J. Liu, Z. T. Liu, L. P. Feng and H. Tian, First-principles study of structural, elastic, electronic and optical properties of rutile GeO_2 and and α-quartz GeO_2, *Solid State Sci.*, 2010, **12**, 1748–1755.

46 G. W. Milton, D. J. Eyre and J. V. Mantese, Finite frequency range Kramers–Kronig relations: bounds on the dispersion, *Phys. Rev. Lett.*, 1997, **79**, 3062–3065.

47 G. Yang and S. P. Gao, A method to restore the intrinsic dielectric functions of 2D materials in periodic calculations, *Nanoscale*, 2021, **13**, 17057–17067.

48 Y. Guo, J. Zhou, H. Xie, Y. Chen and Q. Wang, Screening transition metal-based polar pentagonal monolayers with large piezoelectricity and shift current, *npj Comput. Mater.*, 2022, **8**, 1–9.

49 J. Paier, R. Hirschl, M. Marsman and G. Kresse, The Perdew–Burke–Ernzerhof exchange-correlation functional applied to the G2-1 test set using a plane-wave basis set, *J. Chem. Phys.*, 2005, **122**, 234102.

50 M. Hellenbrandt, The inorganic crystal structure database (ICSD) — Present and future, *Crystallogr. Rev.*, 2014, **10**, 17–22.

51 R. Zacharia, H. Ulbricht and T. Hertel, Interlayer cohesive energy of graphite from thermal desorption of polyaromatic hydrocarbons, *Phys. Rev. B: Condens. Matter Mater. Phys.*, 2004, **69**, 155406.

52 J. H. Jung, C. H. Park and J. Ihm, A rigorous method of calculating exfoliation energies from first principles, *Nano Lett.*, 2018, **18**, 2759–2765.

53 J. Li, X. Fan, Y. Wei and G. Chen, Penta-B_xN_y sheet: A density functional theory study of two-dimensional material, *Sci. Rep.*, 2016, **6**, 31840.

54 E. Cadelano, P. L. Palla, S. Giordano and L. Colombo, Elastic properties of hydrogenated graphene, *Phys. Rev. B: Condens. Matter Mater. Phys.*, 2010, **82**, 235414.

55 C. Lee, X. Wei, J. W. Kysar and J. Hone, Measurement of the elastic properties and intrinsic strength of monolayer graphene, *Science*, 2008, **321**, 385–388.

56 A. D. Becke and K. E. Edgecombe, A simple measure of electron localization in atomic and molecular systems, *J. Chem. Phys.*, 1990, **92**, 5397–5403.

57 G. Henkelman, A. Arnaldsson and H. Jónsson, A fast and robust algorithm for Bader decomposition of charge density, *Comput. Mater. Sci.*, 2006, **36**, 354–360.

58 W. Tang, E. Sanville and G. Henkelman, A grid-based Bader analysis algorithm without lattice bias, *J. Phys.: Condens. Matter*, 2009, **21**, 084204.

59 Y. L Page and P. Saxe, Symmetry-general least-squares extraction of elastic data for strained materials from *ab*

initio calculations of stress, *Phys. Rev. B: Condens. Matter Mater. Phys.*, 2002, **65**, 104104.

60 C. T. Chen, G. L. Wang, X. Y. Wang and Z. Y. Xu, Deep-UV nonlinear optical crystal $KBe_2BO_3F_2$—discovery, growth, optical properties and applications, *Appl. Phys. B*, 2009, **97**, 9–25.

61 S. Grimme, Semiempirical GGA-type density functional constructed with a long-range dispersion correction, *J. Comput. Chem.*, 2006, **27**, 1787–1799.

62 L. Q. Yang, X. M. Jiang and G. C. Guo, $LiGa_{0.54}In_{0.46}S_2$: A new infrared nonlinear optical material with large laser damage threshold designed by gallium substitution in $LiInS_2$, *Inorg. Chem. Commun.*, 2020, **115**, 107852.

63 T. V. Vu, A. A. Lavrentyev, B. V. Gabrelian, D. D. Vo, K. D. Pham, N. M. Denysyuk, L. I. Isaenko, A. Y. Tarasova

and O. Y. Khyzhun, DFT study and XPS measurements elucidating the electronic and optical properties of KPb_2Cl_5, *Opt. Mater.*, 2020, **102**, 109793.

64 H. Lin, L. Chen, J. S. Yu, H. Chen and L. M. Wu, Infrared SHG materials CsM_3Se_6 (M = Ga/Sn, In/Sn): Phase match ability controlled by dipole moment of the asymmetric building unit, *Chem. Mater.*, 2017, **29**, 499–503.

65 P. Makuła, M. Pacia and W. Macyk, How to correctly determine the band gap energy of modified semiconductor photocatalysts based on UV–Vis spectra, *J. Phys. Chem. Lett.*, 2018, **9**, 6814–6817.

66 N. S. Abraham and M. R. Shirts, Thermal gradient approach for the quasi-harmonic approximation and its application to improved treatment of anisotropic expansion, *J. Chem. Theory Comput.*, 2018, **14**, 5904–5919.

This journal is © The Royal Society of Chemistry 2023

J. Mater. Chem. A, 2023, **11**, 167–177 | **177**